Role of Excess Bi on the Properties and Performance of BiFeO$_3$ Thin-Film Photocathodes

DOI:
10.1021/acsaem.3c01926

Document status and date:
Published: 25/12/2023

Document Version:
Publisher's PDF, also known as Version of Record (includes final page, issue and volume numbers)

Please check the document version of this publication:

• A submitted manuscript is the version of the article upon submission and before peer-review. There can be important differences between the submitted version and the official published version of record. People interested in the research are advised to contact the author for the final version of the publication, or visit the DOI to the publisher's website.
• The final author version and the galley proof are versions of the publication after peer review.
• The final published version features the final layout of the paper including the volume, issue and page numbers.

Link to publication

Download date: 08. Feb. 2024

Article

Role of Excess Bi on the Properties and Performance of BiFeO$_3$ Thin-Film Photocathodes

Nitin P. Prasad, Marcus Rohnke, Marcel A. Verheijen, Jacobus M. Sturm, Jan P. Hofmann,* Emiel J. M. Hensen,* and Anja Bieberle-Hütter*

Cite This: ACS Appl. Energy Mater. 2023, 6, 12237−12248

Read Online

ACCESS | Metrics & More | Article Recommendations | Supporting Information

ABSTRACT: BiFeO$_3$ (BFO) has recently been identified as a promising photocathode material for photoelectrochemical (PEC) water splitting due to its light absorption and photoelectrochemical properties. The performance-limiting factors, in particular the impact of stoichiometry on the performance, still need to be understood. The effect of the ratio of Bi/Fe in the precursor solution for sol−gel synthesis on the properties and performance of BFO thin films is investigated in this study. Thin films with a stoichiometric Bi/Fe ratio and with a 10% excess of Bi are prepared on fluorine-doped tin-oxide substrates. While bulk characterization techniques show the formation of phase-pure BFO, surface characterization techniques indicate Bi enrichment on the surface. Light absorption and band gap do not change with excess Bi, whereas the current density is two times higher for Bi excess films compared to stoichiometric films at 0.6 V vs RHE. Electrochemical impedance spectroscopy attributes this improved performance of excess Bi thin films to a lower recombination rate and a lower charge transfer resistance. The lower recombination rate is attributed to fewer Bi and O vacancies, which can act as recombination centers. Therefore, adjusting the Bi/Fe ratio is an effective strategy to enhance the PEC performance of BFO photocathodes.

KEYWORDS: photoelectrochemical water splitting, bismuth ferrite, Bi/Fe stoichiometry, bismuth oxide, vacancies
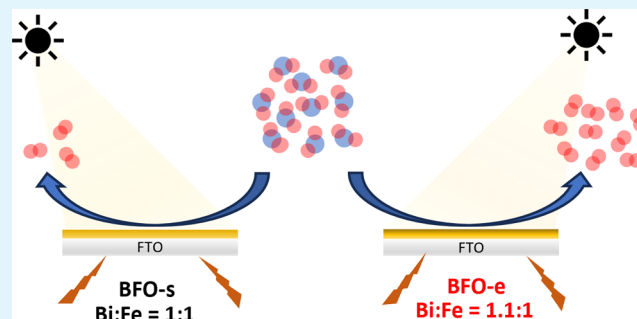
INTRODUCTION

With the rapid increase in worldwide CO$_2$ emissions, there is a need to change from traditional sources of energy to renewable energy.[1] The focus must be on optimizing and improving methods to produce environmentally friendly energy carriers, like hydrogen, to reduce CO$_2$ emissions.[2] Photoelectrochemical (PEC) water splitting is a process to obtain green hydrogen from water driven by solar energy.[3,4] PEC water splitting systems combine solar energy harvesting and water electrolysis in an integrated manner and typically rely on a semiconductor that functions both as a light absorber and as a catalyst.[5] PEC cells consist of two half-electrodes, namely, a photocathode and a photoanode, where the hydrogen evolution reaction (HER) and the oxygen evolution reaction (OER) occur, respectively. Depending on the system, one or both of these electrodes can absorb light.

Several binary and ternary metal oxides have been explored as photoelectrode materials for HER and OER.[5−8] Most of the oxides used as photoelectrodes suffer, however, from limitations, such as poor charge transfer and/or high recombination rates.[9−12] Enhancing charge transfer and reducing recombination rates are therefore important means for increasing the performance of photoelectrodes. Vacancies are an important factor here, since they can act as charge

recombination centers[13] and therefore lower the performance of photoelectrodes in PEC. Thus, it is of great importance to adopt strategies to minimize the negative effect of vacancies on PEC performance.[14]

BiFeO$_3$ (BFO) is a ferroelectric metal-oxide semiconductor that is known to have the largest remanent polarization along the [1 1 1] direction among all known ferroelectric materials.[15] It has been used widely in engineering fields, like electronics[16−18] and spintronics,[19,20] due to the ability to control its ferroelectric domain order by switching the polarization using an external electric field.[21] Due to its favorable band gap of ∼2.7 eV, BFO can also be used for light harvesting in PEC systems.[22,23] Previous studies have shown that BFO is also active for PEC water splitting with several studies emphasizing the role of its ferroelectricity.[24−26] Depending on the synthesis route, pure BFO can be synthesized as either a p-type or an n-type semiconductor.
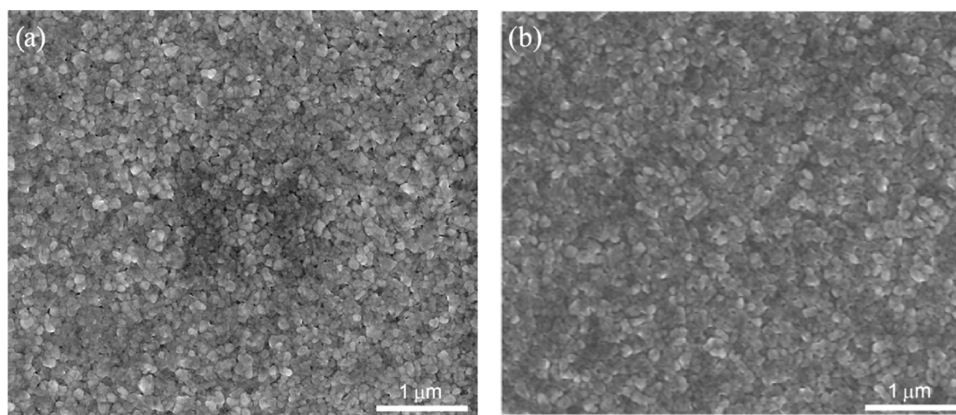
Figure 1. SEM top view images of the surface of BFO thin films synthesized by sol−gel: (a) BFO-s and (b) BFO-e.

Wefring et al. observed that the conductivity of BFO is strongly dependent on the partial pressure of oxygen during the synthesis; decreasing the partial pressure of oxygen leads to a transition from p-type to n-type.[27] Makarovic et al. also show a number of examples from the literature of p-type BFO formed when the annealing was done in air,[28] which supports the results of Wefring et al. Solution-based synthesis that involves annealing in ambient air leads to formation of p-type material, whereas vapor deposition techniques mostly operating under low partial pressures of oxygen (like pulsed laser deposition) form n-type materials.[29] Consequently, BFO can be used as a photocathode[30−33] or photoanode.[24,34−37] Since Bi is volatile, an excess of Bi is often used in the synthesis to compensate for the loss of Bi when subjected to high temperatures.[38−40] However, excess Bi can also lead to the formation of additional phases, like Bi_2O_3 and $Bi_2Fe_4O_9$, which could affect the PEC performance of BFO.[41] A 10% excess of Bi is generally added to compensate for the loss of Bi from thin films during annealing, while at the same time preventing the formation of other phases of the Bi−Fe−O system.[42] On the other side, adding excess Bi is known to beneficially influence the properties of BFO, such as lowering the leakage current,[43] enhancing the polarization by increasing the remanent polarization,[44,45] and reducing the amount of Bi vacancies.[46] While these previous studies have investigated the effect of excess Bi on the material properties and the defect chemistry of BFO thin films, the effect of excess Bi on the PEC performance has not been studied yet. Changes related to different Bi/Fe ratios can impact the PEC performance of BFO thin films as well. Our work aims to study the effect of excess Bi on the PEC properties and performance for HER in p-type BFO thin films prepared by the sol−gel method.

■ RESULTS

To study the effect of excess Bi in BFO photocathodes, thin films of BFO are synthesized on a fluorine-doped tin-oxide (FTO) substrate by a sol−gel method using a precursor solution with a stoichiometric Bi/Fe ratio (BFO-s, Bi/Fe = 1:1 molar ratio) and a 10% excess Bi (BFO-e, Bi/Fe = 1.1:1 molar ratio).

Chemistry and Materials Characterization. *Precursor Characterization.* The concentration of Bi and Fe in the precursor solutions is measured by inductively coupled plasma-optical emission spectroscopy (ICP-OES). The Bi/Fe ratio of the precursor solution used for BFO-s is 0.97, while it is 1.06 for BFO-e (Table S1, see Supporting Information SI-1).

Rutherford backscattering spectroscopy (RBS) is used to determine the bulk composition of the thin films after annealing. Table S2 (Supporting Information SI-2) shows that the bulk Bi/Fe ratios of BFO-s and BFO-e are 0.97 and 1.07, respectively. The good agreement between ICP-OES and RBS results show that the Bi/Fe ratios from the precursor solution are well-transferred to the final thin film.

Morphology. Scanning electron microscopy (SEM) images of the two films (BFO-s and BFO-e) are shown in Figure 1. For both BFO-s and BFO-e, a porous surface structure with round grains of ∼100 nm is observed. No significant difference in the surface morphologies between the two films is found. Both thin films have a thickness of ∼100 nm as observed from cross-sectional SEM images (Figure S1, see Supporting Information SI-3).

Structure and Optical Properties. X-ray diffraction (XRD) patterns are recorded for the thin films to identify the phases formed during annealing and to determine whether Bi-oxide or other Bi−Fe−O phases are formed. Both diffraction patterns in Figure 2 show the characteristic peaks of $BiFeO_3$ along with those of SnO_2 corresponding to the FTO substrate. There are no features due to other phases of the Bi−Fe−O phase diagram.

Figure 3a shows the UV−vis spectra of the thin films BFO-s and BFO-e (measured in transmission mode). The absorption features and intensities of the two films are almost identical. The direct band gap is estimated to be 2.7 eV from the Tauc plots (Figure 3b,c). This band gap is similar to the band gap observed for BFO thin films prepared by solution-based methods in the literature.[47,48] Hence, an excess of Bi does not affect the band gap of the BFO thin films.

Surface Characterization. XPS survey spectra are shown in Figure S2 (see Supporting Information SI-4). In addition to Bi, Fe, and O from BFO, C is detected as a typical impurity from sample handling and preparation in air. Neither Sn nor F is observed in the survey spectra. This indicates that diffusion of these elements from the FTO substrate to the surface of the thin films does not take place.

The Bi/Fe ratio on the surface of the thin films can be calculated by estimating the area of the Bi and Fe XPS spectra, as shown in Figure 4. Taking into account only Bi and Fe XPS spectra, the surface of BFO-s is estimated to contain 50.4% Bi and 49.6% Fe, resulting in a Bi/Fe ratio of 1.01. This is very close to the expected value of 1. BFO-e contains 55.1% Bi and 44.9% Fe resulting in a ratio of Bi/Fe at the surface of 1.23, which is significantly higher than the expected value of 1.1.
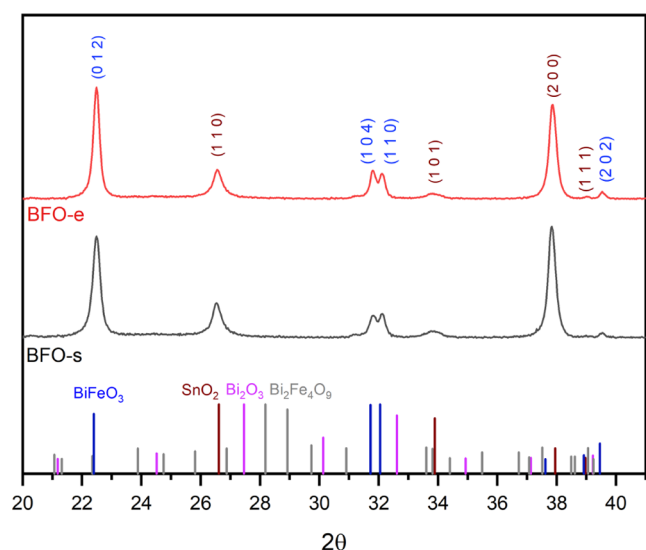
Figure 2. XRD pattern of BFO thin films with stoichiometric (BFO-s, black) and excess Bi (BFO-e, red). The peak positions of SnO_2 (PDF 00-041-1445), Bi_2O_3 (PDF 00-045-1344), $Bi_2Fe_4O_9$ (PDF 01-074-1098), and $BiFeO_3$ (PDF 01-072-7678) are marked. The thin films consist of a pure BFO phase; SnO_2 peaks are related to the FTO substrate.

This result is an indication that Bi segregates to the surface of the BFO thin films.

XPS data can also be used to obtain information about the oxidation states of Bi and Fe at the surfaces of the thin films. The Bi 4f spectra for the BFO-s and BFO-e thin films in Figure 4a show the Bi $4f_{7/2}$ peak at ~158.5 eV due to Bi^{3+}.[49,50] Features due to metallic Bi, which would appear at a Bi $4f_{7/2}$ binding energy of 157.0 eV, are not observed. Vacancies can have an effect on the XPS spectra since they change the local chemical environment around an atom. A slight shift of Bi peaks toward lower binding energy indicates the presence of lower valent Bi ions ($Bi^{(3-x)+}$).[51] Such a shift of BFO-s toward lower binding energies as compared to BFO-e is observed by Yang et al. on adding different amounts of excess Bi (0−7%) in BFO thin films.[52] The Fe 2p spectra shown in Figure 4b contain peaks corresponding to Fe $2p_{3/2}$ (~710.0 eV) along with two corresponding satellite peaks at ~718.5 and ~732.0 eV. The position of the satellite peak can be used to identify

the oxidation state of Fe[53] and confirms the presence of Fe^{3+} in both films.[54]

The O 1s XPS spectra of BFO-s and BFO-e thin films are shown in Figure 5. The spectra are fitted with three contributions. The first feature (Peak 1; BFO-s: 529.5 eV; BFO-e: 529.6 eV) corresponds to lattice oxygen from BFO.[55] The second feature (Peak 2; BFO-s: 531.0 eV; BFO-e: 531.1 eV) is attributed by some reports to oxygen adjacent to an oxygen vacancy (also referred to by some literature as dangling oxygen bonds), while others attribute this feature to hydroxyl species adsorbed on the surface.[56,57] Sometimes this feature is also erroneously attributed to oxygen vacancies directly.[58,59] Idriss emphasized that this feature corresponds to hydroxyl species adsorbed to the surface of metal oxides and discarded the role of oxygen vacancies as these would be readily oxidized when exposed to air.[56] Nevertheless, these hydroxyl species might still be indicative of the occurrence of surface oxygen vacancies, since such vacancies can be readily oxidized by strongly adsorbing water under ambient conditions.[56] The feature with the highest binding energy (Peak 3; BFO-s: 532.3 eV; BFO-e: 532.4 eV) represents adsorbed oxygen species, which might also arise from the healing of vacancies under ambient conditions. In this sense, the two high-energy peaks are representative of the amount of oxygen vacancies.[60,61] Under this assumption, the amount of oxygen vacancies relative to lattice oxygen is determined and listed in Table S4 (see Supporting Information SI-5). According to this data, BFO-e contains less oxygen vacancies than BFO-s, which is reasonable as the addition of excess Bi can be expected to lower the number of oxygen vacancies in the BFO thin film. A slight shift toward lower binding energy (≤0.1 eV) is observed for the O 1s spectra of BFO-e as compared to BFO-s. Compared with the literature, these shifts are within the error range of XPS reported for BFO thin films.[46]

XPS can also be used to estimate the band positions of BFO-s and BFO-e as described in Supporting Information SI-6. The position of the Fermi level (E_F) is estimated as 4.4 and 4.9 eV for BFO-s and BFO-e, respectively. The valence band maxima (VBM, E_{VB}) obtained from XPS valence band spectra for BFO-s and BFO-e are 5.9 and 6.2 eV, respectively. Using the band gap (2.7 eV for both BFO-s and BFO-e) obtained from UV−vis spectroscopy, the conduction band minima (CBM, ECB) are calculated to be at 3.2 and 3.5 eV for BFO-s and BFO-e, respectively. The complete band diagrams of BFO-s and BFO-

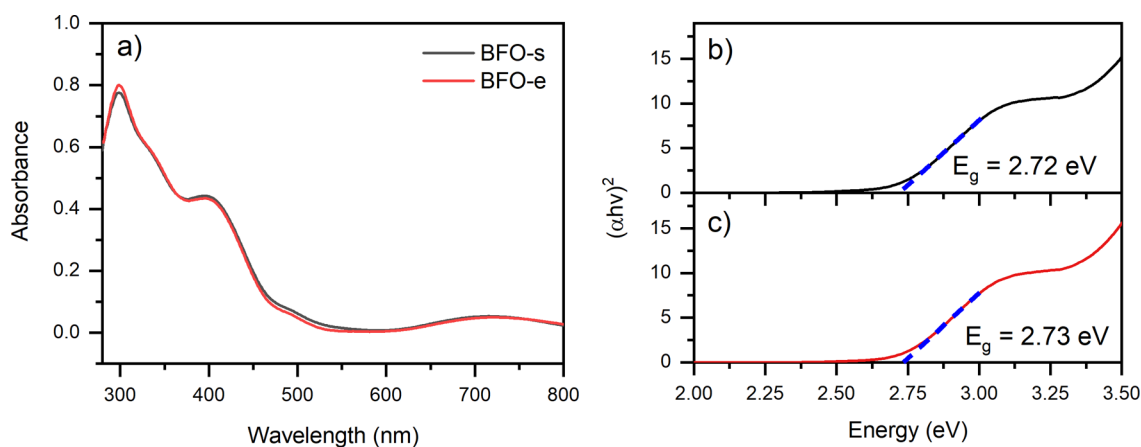
Figure 3. UV−vis spectra of BFO thin films with different Bi/Fe ratios. (a) UV−vis spectra of BFO-s and BFO-e thin films. Tauc analysis of thin films prepared from (b) BFO-s and (c) BFO-e. The band gaps of both films are derived to be 2.7 eV.
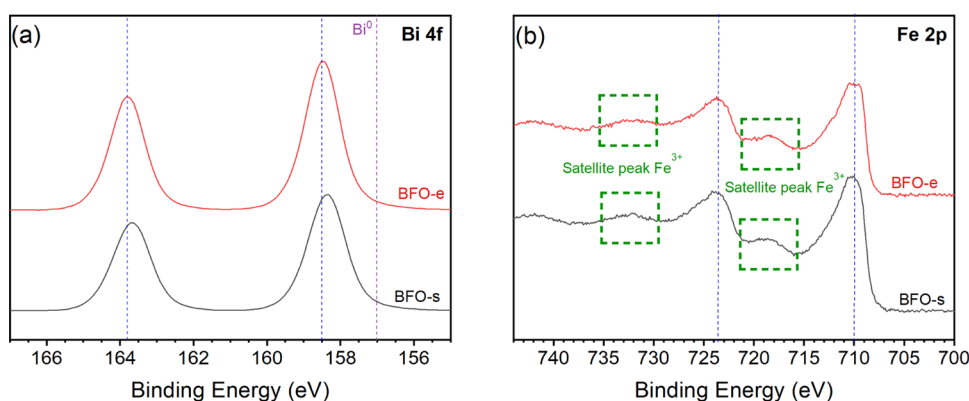
Figure 4. (a) Bi 4f and (b) Fe 2p XPS spectra of BFO-s thin films with stoichiometric Bi/Fe (black) and BFO-e with excess Bi in the precursor solution (red).
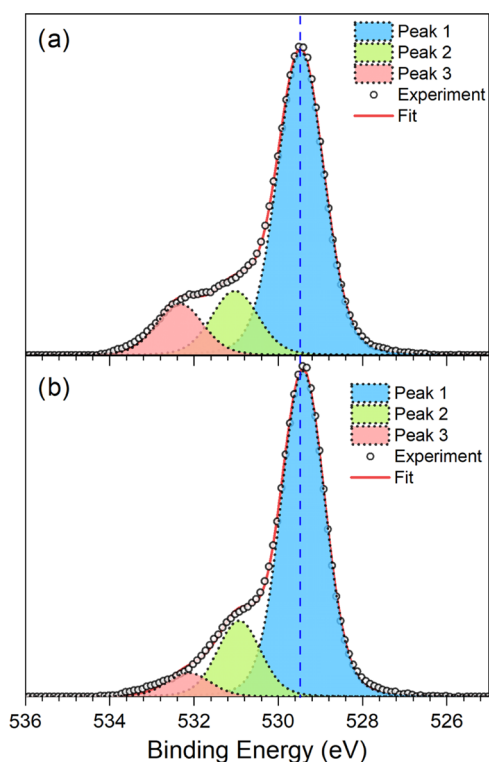

Figure 5. O 1s spectra of (a) BFO-s and (b) BFO-e along with fitting based on three peak models. The amount of oxygen vacancies is calculated based on the areas of the constituent peaks; the results are presented in Table S4.

e are shown in Figure 6. The conduction bands of both BFO-s and BFO-e lie above the thermodynamic potential of HER at 4.5 eV, suggesting that both materials are capable of producing hydrogen. It can also be observed that the Fermi level of BFO-s is closer to its conduction band ($\Delta = 1.2$ eV) than that of the BFO-e band ($\Delta = 1.4$ eV), which could be an indication for the presence of oxygen vacancies in BFO-s.

To more accurately analyze the top surface of the thin films, the XPS measurements are complemented by low-energy ion scattering (LEIS), which has a probing depth of a few monolayers.[62] LEIS spectra for BFO-s and BFO-e are shown in Figure 7 along with reference spectra for Bi-oxide and Fe-oxide, which are prepared by the same sol−gel method as BFO-s and BFO-e. Comparing the spectra of the Bi- and Fe-oxide, it is found that the peak at ~2700 eV is observed only

for the Bi-oxide, which suggests that this peak corresponds to Bi. The peak at ~2200 eV is only present in the Fe-oxide and is absent in the Bi-oxide. Therefore, this peak is considered as the characteristic peak for Fe. The peak at ~1100 eV is observed in all spectra (BFO-s, BFO-e, Bi-oxide, Fe-oxide), which indicates that this peak is characteristic of oxygen. Comparing the spectra of BFO-s and BFO-e, it is found that both BFO thin films have a strong Bi peak (~2700 eV), whereas no clear Fe peak (~2200 eV) is found. This confirms our indication from XPS elemental composition that the top surface is highly Bi-rich and has a negligible amount of Fe.

Bulk Film Composition. To ascertain whether Bi segregation is limited to the surface or occurs in the bulk of the thin films, time-of-flight secondary ion mass spectroscopy (ToF-SIMS) is performed coupled with depth profiling. The intensities of Bi and Fe detected as a function of depth are shown in Figure 8a,b. For both thin films, BFO-s and BFO-e, the intensity of Bi (blue curve) is very high at the surface, decreases strongly within the first few nanometers (0−2 nm), then increases slightly (2−10 nm), and afterward stays rather constant. The concentration of Fe (green curve), in contrast, increases in the first ~10 nm and stays constant thereafter. Hence, the ToF-SIMS results confirm that Bi is segregated to the surface of both thin films in line with observations from LEIS. Figure 8c shows the Bi/Fe ratio of the two thin films as a function of the film thickness. The Bi/Fe ratio is similar for BFO-s and BFO-e up to ~2 nm. As we go deeper into the thin films, BFO-e has a Bi/Fe ratio higher than that of BFO-s. This indicates that the top surfaces of BFO-s and BFO-e are Bi-rich and have similar Bi/Fe ratios. It is important to note that this ratio cannot be compared to the actual Bi/Fe ratio measured by XPS or RBS, since the intensities of Bi and Fe in ToF-SIMS (Figure 8c) are absolute counts and are not calibrated. Nevertheless, a comparison between the samples is still possible.

In order to further investigate the distribution of Bi and Fe in the cross section of the thin films, lamella of the thin films were prepared by a focused ion beam and were analyzed by scanning transmission electron microscopy (STEM) along with energy dispersive X-ray spectroscopy (EDX). Figure 9 shows the individual (Figure 9a−c) and combined elemental mappings (Figure 9d) of Bi, Fe, and O in BFO-s. In the combined elemental distribution (Figure 9d), a distinct layer of Bi (green) is found at the surface of BFO-s. A thin layer of Fe (red) can be seen below Bi (green). These layers are followed by the region where both Bi and Fe are present. O is observed
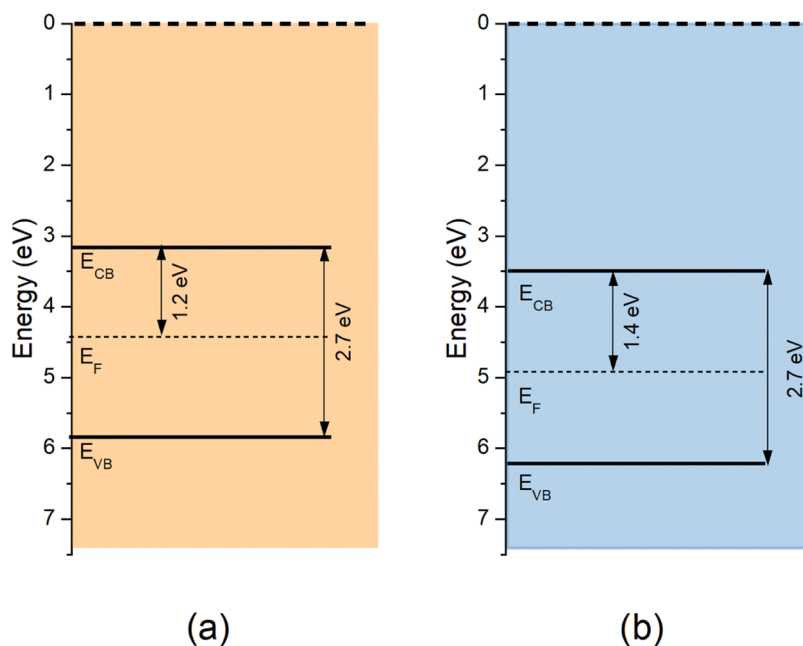
Figure 6. Band energy diagram constructed from XPS and UPS measurements showing the valence band (E_{VB}), Fermi level (E_F), and conduction band (E_{CB}) of (a) BFO-s and (b) BFO-e thin films.
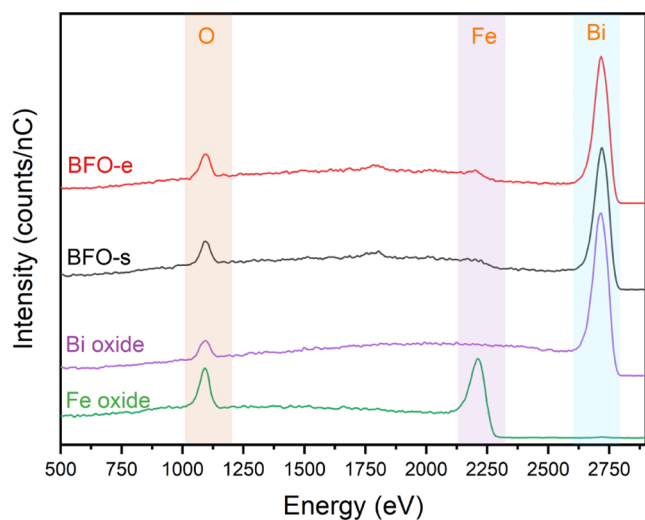

Figure 7. Low-energy ion spectroscopy (LEIS) spectra of BFO-s, BFO-e, Bi-oxide, and Fe-oxide. Shadowed areas indicate the peak positions of Bi, Fe, and O.

throughout the thin film, even in the layers where only Bi or only Fe are observed. The individual Bi and Fe distributions also complement this observation. Similar observations are also found for BFO-e as shown in Figure S3 (see Supporting Information SI-7). Thus, TEM-EDX confirms the surface segregation of Bi that was observed by ToF-SIMS.

Photoelectrochemical Characterization. *Photoelectrochemical Performance.* Photoelectrochemical performance is measured in a three-electrode setup with 0.1 M Na$_2$SO$_4$ as the electrolyte (pH = 6.5) by performing linear sweep voltammetry (LSV) in the dark and under illumination. As seen in Figure 10, both films exhibit a negligible dark current (dashed lines). Under illumination (solid lines), BFO-e has a current density that is higher than that of BFO-s over the entire range of applied potentials. At 0.6 V vs RHE, the current density under illumination for BFO-e photoelectrode is nearly two times higher than that of the BFO-s thin film. Figure S6 (see Supporting Information SI-8) displays chopped light voltammetry measurements of BFO-s and BFO-e in different electrolytes. In all electrolytes, BFO-e has a higher current density than BFO-s although there is a difference in the absolute current density measured in each electrolyte. Figure
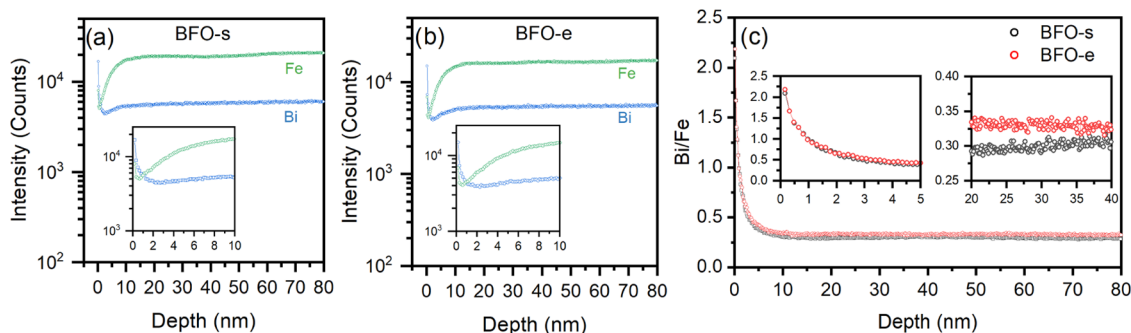

Figure 8. Time-of-flight secondary ion mass spectroscopy (ToF-SIMS) measurement of Bi and Fe as a function of etch depth of (a) BFO-s and (b) BFO-e along with the (c) Bi/Fe ratio. Bi segregation takes place at the surfaces of both films.
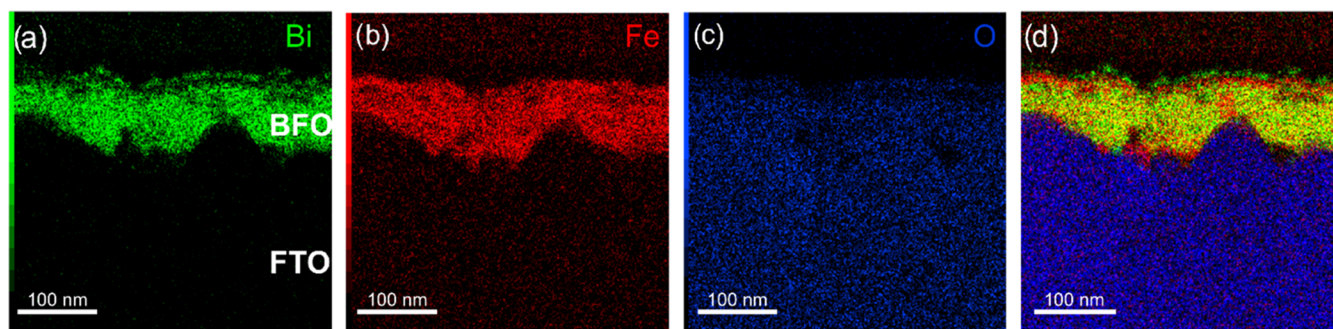
Figure 9. Cross-sectional STEM-EDX elemental mappings of BFO-s showing (a) Bi distribution, (b) Fe distribution, (c) O distribution, and (d) combined Bi, Fe, and O elemental distribution. A thin Bi-oxide (green) layer is observed at the surface followed by an Fe-oxide (red) layer underneath.
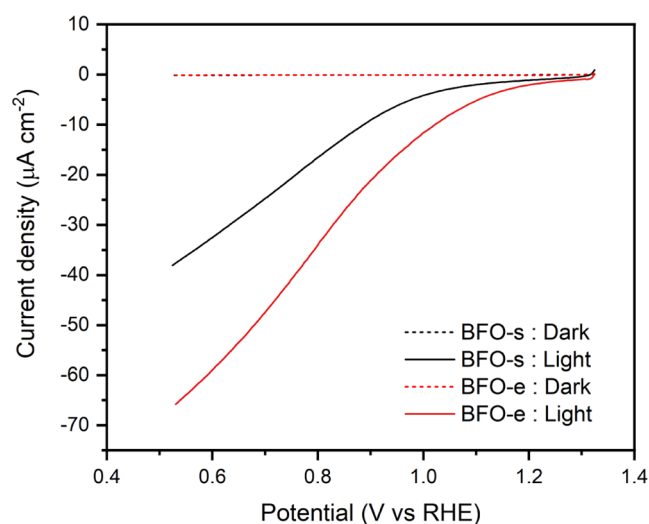

Figure 10. Linear sweep voltammetry in the dark (dashed lines) and under illumination (solid lines) for BFO-s and BFO-e photoelectrodes. Higher performance under illumination is observed for the BFO-e thin film as compared to the BFO-s thin film. White LED light with an intensity of 100 mW cm^{-2} is used as the illumination source and 0.1 M Na$_2$SO$_4$ is used as the electrolyte.

S6a shows the chopped light voltammetry in the presence of H$_2$O$_2$ as an electron scavenger added to the same electrolyte as Figure 10. This is done in order to reduce the probability of recombination at the surface due to sluggish reaction kinetics (thereby removing surface limitation, if any) and to compare the photoelectrodes based on processes occurring in the bulk of the materials. It is found that even in the presence of H$_2$O$_2$, the performance of BFO-e is better than that of BFO-s. Moreover, the total current density of the BFO-e thin film in the presence of H$_2$O$_2$ is higher compared to the current density recorded in its absence (compare the *y*-axis in Figure 10 with Figure S6a). The same trend is found for BFO-s. This suggests that some surface limitation affects the photocurrent response in BFO thin films irrespective of their Bi/Fe stoichiometry.

Electrochemical Impedance Spectroscopy. To further understand the reason for the better PEC performance of BFO-e, the charge transfer properties during PEC operation are studied by electrochemical impedance spectroscopy (EIS) in the potential range of 1.3−0.5 V vs RHE with an interval of 0.1 V under illumination (see Supporting Information SI-9, Figure S7). The Nyquist plots of BFO-s and BFO-e at a potential of 0.5 V vs RHE are shown in Figure 11a. Both Nyquist plots show two features in the form of semicircles,
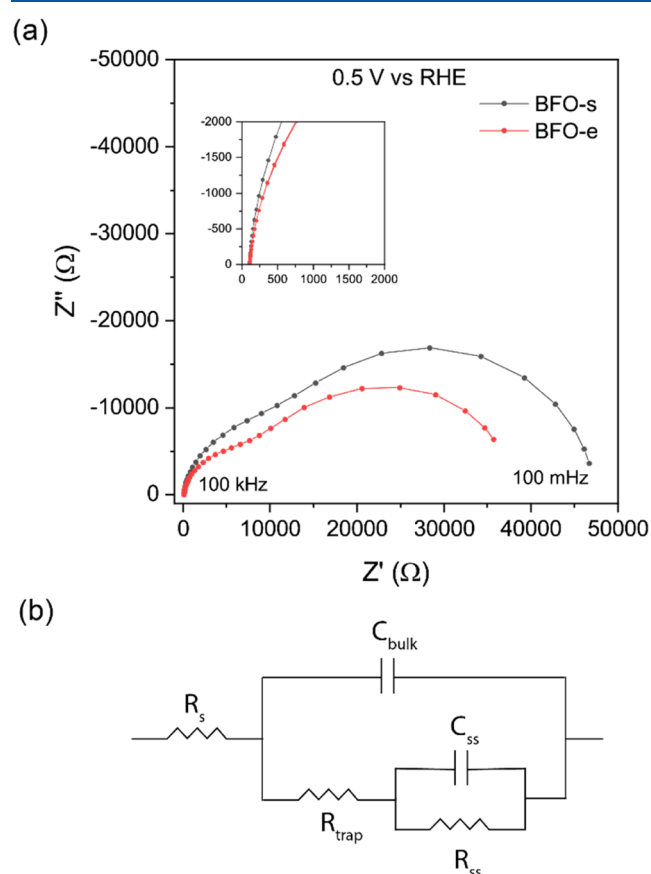
Figure 11. (a) Electrochemical impedance spectroscopy (EIS) data of BFO-s and BFO-e at 0.5 V vs RHE under 100 mW cm^{-2} illumination in 0.1 M Na$_2$SO$_4$; Inset: High-frequency region of Nyquist plot. (b) Equivalent circuit model for fitting of the EIS data.

which can be assigned to two different charge-transfer-related processes. To decouple these processes, the EIS data are fitted with the equivalent circuit model (ECM) shown in Figure 11b. This ECM, which is commonly used for photoelectrodes,[63−66] consists of three resistances and two constant phase elements. R_s refers to the series resistance related to the back-contact between the BFO and the FTO substrate along with the electrolyte resistance. The trapping resistance, R_{trap}, is associated with charge carrier recombination at surface states

such as vacancies. Higher R_{trap} indicates that more charges are trapped at surface states, and therefore more charge recombination can take place. R_{ss} refers to the resistance of charge transfer from the surface state to the electrolyte. The bulk capacitance of the BFO thin film is expressed as C_{bulk} and the capacitance related to the surface states is represented by C_{ss}.

The fitting results of the resistances are shown in Figure 12. Resistances related to BFO-s are, in general, higher than those

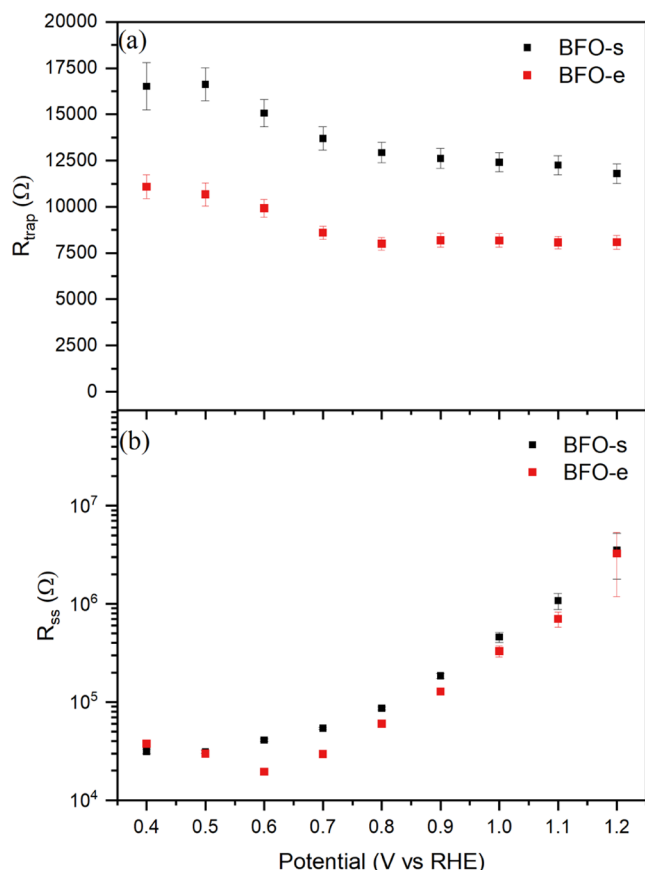**Figure 12.** Comparison of (a) trapping and detrapping resistance (R_{trap}) and (b) charge transfer resistance from surface states for HER (R_{ss}) for BFO-s and BFO-e as obtained from fitting the electrochemical impedance spectroscopy data with the equivalent circuit shown in Figure 11b.

related to BFO-e (Figure 12a). The higher R_{trap} of BFO-s compared to BFO-e (Figure 12a) indicates that more charges are trapped at the surface states, which can lead to increased charge recombination and result in a lower PEC activity. Thus, introducing a slight excess of Bi into the precursor solution seems to reduce the surface states and, by this, results in less charge recombination.

R_{ss} is also considerably lower for BFO-e compared to BFO-s (note the logarithmic scale of the y-axis, Figure 12b). Hence, with extra Bi in the precursor solution, the resistance of charge transfer from the semiconductor surface to the electrolyte is lowered. This effect is further confirmed by EIS measurements in the presence of an electron scavenger (Figure 13). Compared to Figure 11a, the presence of an electron scavenger in the electrolyte leads to a single arc in the Nyquist plot in Figure 13, indicating only a single charge-related process. One of the semicircles (related to R_{trap} at lower frequencies) in
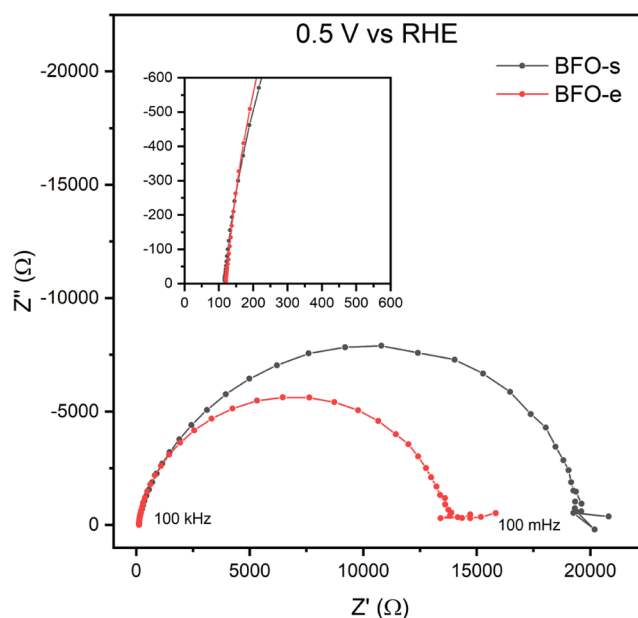

Figure 13. Photoelectrochemical impedance spectroscopy at 0.5 V vs RHE for BFO-s and BFO-e thin films in 0.1 M Na_2SO_4 in the presence of H_2O_2 as an electron scavenger.

Figure 11a disappears in Figure 13 since the limitations due to sluggish surface kinetics are removed. The arc in the Nyquist plot is smaller for BFO-e compared to BFO-s. This indicates that the resistance to charge transfer in the presence of an electron scavenger is also lower for BFO-e. Therefore, it can be summarized that excess Bi not only reduces charge recombination but also lowers the charge transfer resistance for HER.

■ DISCUSSION

The PEC characterization (Figures 10−13) clearly shows that the BFO-e thin films perform better than the BFO-s: about 1.5 times higher current density at an applied potential of 0.5 V vs RHE was found for BFO-e compared to BFO-s as well as a smaller impedance with lower R_{trap} and R_{ss}. These results can be explained by means of chemical and materials characterization as summarized in Figure 14. Mainly two reasons explain the improved PEC activity of BFO-e compared to BFO-s.

First, the presence of Bi-oxide at the surface improves the charge transfer toward HER (left part of Figure 14): LEIS (Figure 7) and TEM (Figure 9) analyses clearly showed that Bi oxide is present at the topmost surface of the thin films irrespective of the Bi/Fe ratio. TEM analysis could visualize a Bi-oxide layer on the top, followed by a subsurface Fe-oxide layer. To the best of our knowledge, this is the first time that separate Bi- and Fe-oxide layers are observed on the surface of BFO thin films prepared by a sol−gel method. XPS analysis (from Figure 4) showed that BFO-e has a higher Bi content compared to Fe. This is an indirect measure for a Bi-rich surface. Note that XRD analysis (Figure 2) does not detect distinct oxide layers, since most likely the volume of the surface layer is very small as compared to that of the bulk, thereby making the peaks of the surface layers broad, very low in intensity, and hence not detectable. Hence, TEM, LEIS, and XPS all find a Bi-rich layer, mainly the Bi-oxide layer at the surface of the thin films, which is known to improve the charge transfer.[66,67] As LEIS is a more surface-sensitive technique
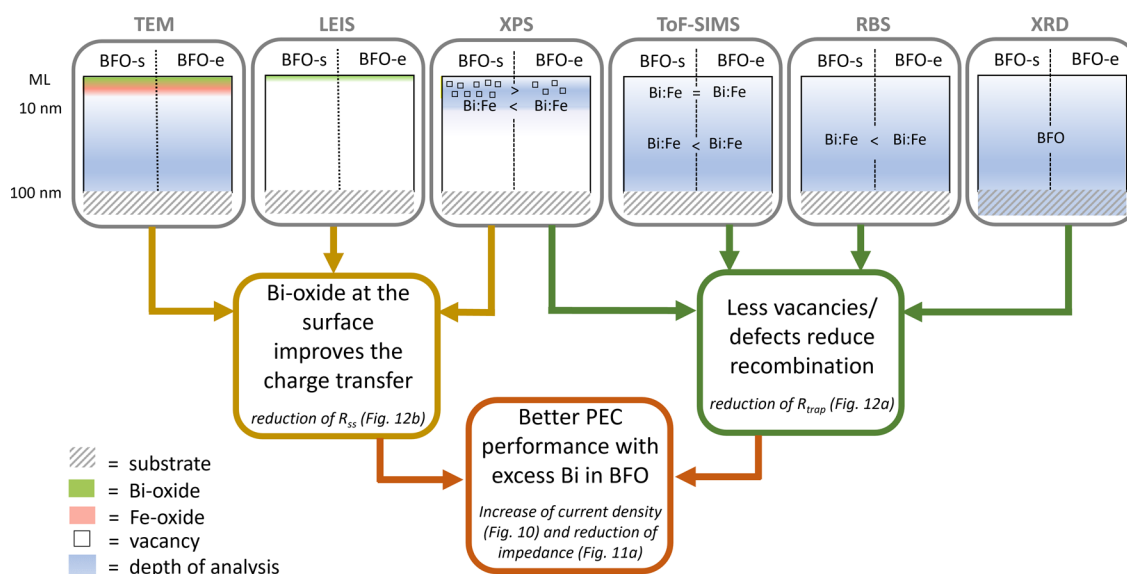
Figure 14. Summarizing sketch to explain the improved PEC performance of BFO-e compared to BFO-s. The higher performance is attributed to a combined effect of Bi-oxide at the surface improving the charge transfer and less vacancies reducing recombination. Yellow marking illustrates the depths of analysis, shaded area is the substrate.

compared to XPS, the Fe observed in XPS spectra is barely seen in the LEIS spectra of BFO thin films. This further confirms that the topmost layer is almost entirely Bi-oxide. Hence, the reduction of R_{ss} in Figure 12b, which is related to a smaller impedance, could be related to the formation of a Bi-oxide layer on the top of the thin film. The Bi/Fe ratio from the XPS composition analysis of BFO-e is higher than the expected ratio when compared to BFO-e, which possibly suggests that BFO-e has a thicker Bi-oxide layer compared to BFO-s. The lower R_{ss} results in a higher current density and thus explains the higher current density of BFO-e under illumination compared to BFO-s.

Second, less vacancies reduce the electron−hole recombination (right part of Figure 14). Vacancies in a materials can be a location for electrons and holes to recombine and thus reduce the current density and therefore the performance.[68,69] According to XPS analysis (from Figure 5), BFO-e has fewer vacancies than BFO-s in the measurement depth of XPS of about 2 nm. XPS spectra (Figure 4a) show that the Bi 4f peak shifts toward lower binding energies for BFO-s as compared to BFO-e, indicating lower valent Bi ions in BFO-s. This could be a result of the formation of oxygen vacancies in BFO-s due to the breaking of the Bi−O bond.[51] Cation and anion vacancies tend to occur in pairs (Schottky defect) in BFO,[70,71] and therefore, less Bi vacancies translate also to less O vacancies. In agreement with this, peak fitting of the O 1s XPS spectra indicated that the number of oxygen vacancies is higher for BFO-s. Shifting of the Fermi level toward the conduction band in BFO-s as compared to BFO-e is also an indication of oxygen vacancies being present in BFO-s. The presence of donor levels due to oxygen vacancies can shift the Fermi level toward the conduction band.[72,73] Less vacancies are indirectly also found in the bulk of the materials by means of ToF-SIMS (Figure 8), RBS (Supporting Information SI-2), and XRD (Figure 2). Both ToF-SIMS and RBS indicated a higher Bi/Fe ratio in BFO-e along with fewer bismuth and oxygen vacancies (Schottky defects) for BFO-e as compared to BFO-s as seen from XPS (from Figure 5). These observations are in agreement with Yang et al. who found that having a thin

film prepared by pulsed laser deposition from a target with excess Bi leads to the reduction in oxygen vacancies.[46] XRD found a pure BFO phase within the detection limit of this method. No other phase was detected, which indirectly confirms that no large number of vacancies exist in the bulk of the thin films. Hence, in summary, BFO-e is indicative of higher Bi content and, directly and indirectly, of less vacancies. This leads to less recombination and therefore reduces R_{trap} (Figure 12a) and results in higher PEC activity.

■ CONCLUSIONS

The Bi−Fe stoichiometry is found to play an important role in the performance of BFO thin films for PEC hydrogen evolution. Stoichiometric and Bi-rich thin films prepared by the sol−gel method and high-temperature annealing exhibit the identical Bi/Fe ratio as the corresponding precursor solutions. Distinct Bi oxide and Fe-oxide layers are visualized for the first time at the surface of BFO thin films prepared by the sol−gel method. It is found that a 10% excess of Bi in the precursor solution improves the PEC performance of BFO thin films by almost 50% as compared to thin films with a stoichiometric Bi/Fe ratio in the precursor solution. The excess Bi does not affect light absorption, surface morphology, or phase formation. The better performance of the Bi-rich thin film is attributed to (1) the presence of Bi-oxide at the surface, which improves the charge transfer toward HER, and (2) less oxygen and Bi vacancies (Schottky defects), which reduce the electron−hole recombination. Both effects lead to a higher PEC performance of the excess Bi thin film.

In summary, it is shown that stoichiometry plays a crucial role in the performance of photoelectrodes, and tuning the stoichiometry can significantly improve the performance of thin-film photoelectrodes for PEC water splitting applications. This finding is of particular importance regarding the use of ternary or quaternary metal-oxide materials for PEC applications. The performance of BFO with excess Bi can be further improved by using an electrolyte of higher molarity and optimizing the anode catalyst. In-depth understanding of it and how the presence of a very thin Bi-oxide layer on top of BFO

thin films (as observed in this study) affects the ferroelectricity could also be beneficial for the application of BFO in other fields.

EXPERIMENTAL METHODS

Cleaning of Substrates. FTO glass (NSG TEC 15 on 1.3 mm glass) of 2 cm × 2 cm was sonicated in Milli-Q water, acetone, and isopropanol for 20 min each. Edges of the FTO were masked using Scotch brand tape for realizing electrical contact in PEC measurements. Finally, the substrates were subjected to ozone cleaning (Ossila UV Ozone Cleaner) for 20 min.

Synthesis of the BiFeO₃ Precursor. BiFeO₃ thin films with varying Bi—Fe stoichiometry were synthesized using the sol—gel-based spin-coating method. Two different Bi/Fe ratios were used: 1.0:1 (BFO-s) and 1.1:1 (BFO-e). The precursor solution for spin-coating was prepared as described by Zhang et al.[74] The total concentration of the metal ions in the precursor solution was fixed for all stoichiometries at 0.5 M. Based on the stoichiometry, the required amounts of $Bi(NO_3)_3 \cdot 5H_2O$ (99.95%, Sigma-Aldrich) and $Fe(NO_3)_3 \cdot 9H_2O$ (99.99%, Sigma-Aldrich) were dissolved in 8 mL of 2-methoxyethanol (99.8%, Sigma-Aldrich). The solution was kept on a magnetic stirrer to aid the dissolution of the salts. Once the salts were fully dissolved, 4 mL of acetic anhydride was added. On adding the acetic anhydride, the solution heats up due to the exothermic reaction between 2-methoxyethanol and acetic anhydride. The solution was allowed to cool down before using it for spin-coating. The solutions are in principle stable for up to 2 weeks; however, it this study, they were always used within 5 days of preparation.

Synthesis of BiFeO₃ Thin Films. 0.5 mL portion of the precursor solution was spin-coated onto a cleaned FTO substrate. Spin-coating was performed using a Polos 150i Spin Coater. The substrate was held onto the spin-coater by using vacuum. The spin-coating program consisted of two steps. Deposition of the precursor solution was done at 1500 rpm for 30 s, followed by the thinning step at 3000 rpm for 20 s. Immediately after spin-coating, the samples were dried for 2 min at 100 °C on a hotplate. The dried samples were then transferred to an oven (Nabertherm) where they were annealed at 270 °C for 5 min in air to allow the remaining solvent to evaporate. This was followed by annealing at 550 °C for 2 h. All ramp rates were set to the highest possible ramp rate of the machine (which can be achieved by setting the ramp time to 0). The samples were allowed to cool naturally in the oven. This entire cycle from spin-coating to annealing and then cooling was repeated for each spin-coating step. All films in this study consisted of four spin-coating cycles with a thickness of ∼100 nm.

Structure, Morphology, and Optical Characterization. X-ray diffraction (XRD) patterns were recorded with a Bruker D2 PHASER diffractometer using Cu Kα radiation for 2θ values from 20 to 40°. X-ray photoemission spectra (XPS) were recorded with a Thermo Scientific K-α spectrometer using an Al Kα source. A spot size of 400 μm in diameter was used for all measurements. All spectra were calibrated using the adventitious carbon (AdC) 1s set to 284.8 eV and analyzed using CasaXPS. An electron flood gun was used to compensate for charging of samples. UV—visible spectroscopy measurements were performed in transmission mode by a PerkinElmer 1050 UV/vis/NIR spectrophotometer with scans from 800 to 280 nm with steps of 1 nm. Scanning electron microscopy (SEM) images were taken by using a field emission scanning electron microscope (Zeiss Sigma) with an in-lens detector and 10 kV accelerating voltage.

Low-Energy Ion spectroscopy (LEIS). LEIS spectra were acquired with a high-sensitivity LEIS spectrometer of the type Qtac100 supplied by IONTOF GmbH (Münster, Germany). After introducing the samples in vacuum, the samples were treated with atomic oxygen in the load-lock of the LEIS setup in order to remove hydrocarbon contamination. Atomic oxygen was generated by a Specs MPS-ECR plasma source operating at a process pressure of 5×10^{-5} mbar O_2, and each sample was treated for 10 min. All LEIS measurements were performed with a 3 keV He⁺ beam normally incident on the sample at a fixed scattering angle of 145°. The primary

beam current, typically around 3 nA, was measured with a Faraday cup directly before the LEIS measurement. The analysis area was set to 1×1 mm² by rastering the ion beam; a typical fluence of around 3×10^{14} He⁺ ions per cm² was used for a single measurement.

Time-of-Flight Secondary Ion Mass Spectroscopy (ToF-SIMS). Mass spectrometric analysis of the thin films was carried out by time-of-flight secondary ion mass spectrometry (ToF-SIMS). Here, an M6 Hybrid SIMS (IONTOF GmbH, Muenster, Germany) was used. The machine is equipped with a 30 keV Bi cluster nanoprobe for analysis and a 2 kV electron impact ionization gun for sputtering. The Bi emitter consists of a BiMn alloy and within the first hundred hours of operation, the Mn content is sufficient to form a Mn⁺ primary ion beam, which was applied for analysis of the Bi-containing samples. The analysis current was about 0.364 pA at a cycle time of 75 μs. For depth profiling, a 500 eV O_2^+ ion beam was scanned over an area of 300×300 μm² with an beam current of 95.5 nA. The analysis was carried out in an area of 150×150 μm² centered to the sputter beam (256×256 pixels, 2 frames/patch). Analysis and sputter gun operated in noninterlaced mode with eight sputter frames between the analysis scans and 0.5 s pause time for charge compensation by a low energetic electron gun before each analysis scan. After SIMS depth profiling, crater depths were measured with a profilometer (α-Step D600, KLA Tencor, Milpitas, USA). The depth information was used for calibration of the sputter time axis. Data evaluation was carried out with Surface Lab 7.2 software (IONTOF GmbH, Muenster, Germany).

Cross-Sectional Transmission Electron Microscopy. Cross-sectional TEM samples were prepared by using a Nova Nanolab Dualbeam (FEI, Netherlands) following a standard lift-out sample preparation protocol. Subsequent TEM studies were performed using a probe-corrected JEOL ARM200F transmission electron microscope (TEM) operated at 200 kV in high-angle annular dark field (HAADF) scanning TEM (STEM) mode, combined with a 100 mm² SDD EDX detector.

Photoelectrochemical Measurements. Photoelectrochemical measurements were performed in a standard three-electrode configuration using a Zahner Elektrik GmbH IM6 potentiostat with a PP211 light controller. PEC measurements were performed in a Zahner PECC-2 cell with a 0.7 cm diameter area exposed to the electrolyte. Pt wire was used as the counter electrode and Ag/AgCl (3 M NaCl) electrode as the reference electrode (E_{ref} = 0.23 V vs SHE). 0.1 M Na₂SO₄ was used as the electrolyte (pH = 5.6). In the case of measurements with an electron scavenger, 0.5 mL of H₂O₂ was added to the electrolyte in the cell before measurements. A white LED source with an intensity of 100 mW cm⁻² was used for illumination. All voltammetry measurements were performed with a scan rate of 25 mV s⁻¹. Chopped light cycles of 1 s of light on and 1 s of light off were used for the voltammetry measurements. All potentials were reported vs RHE using the formula: $V_{RHE} = V_{Ag/AgCl} + 0.23$ V $+ 0.0591$ V * pH.

Electrochemical Impedance Spectroscopy (EIS). Electrochemical impedance spectroscopy measurements were performed using a Zahner Elektrik GmbH IM6 potentiostat with a PP211 light controller. The DC potential was varied from 1.2 to 0.4 V vs RHE. The amplitude of AC voltage was 10 mV and the frequency was varied from 100 kHz to 100 mHz. The photocathode was held at each potential for 1 min before an EIS measurement was recorded. After the EIS was recorded at one potential, a 10 min delay was included before measuring the EIS at the next potential. All measurements were done under illumination using a white LED source with an intensity of 100 mW cm⁻².

ASSOCIATED CONTENT

ⓈI Supporting Information

The Supporting Information is available free of charge at https://pubs.acs.org/doi/10.1021/acsaem.3c01926.

> ICP-OES, RBS, SEM thickness, XPS survey spectra, vacancy calculation from O 1s spectra, band energy positions calculations, STEM-EDX, PEC in different

electrolytes, and electrochemical impedance spectroscopy ([PDF](#))

■ AUTHOR INFORMATION

Corresponding Authors

Jan P. Hofmann − *Laboratory of Inorganic Materials and Catalysis, Department of Chemical Engineering and Chemistry, Eindhoven University of Technology, 5612 AE Eindhoven, The Netherlands; Surface Science Laboratory, Department of Materials and Earth Sciences, Technical University of Darmstadt, 64287 Darmstadt, Germany;* orcid.org/0000-0002-5765-1096; Email: hofmann@surface.tu-darmstadt.de

Emiel J. M. Hensen − *Laboratory of Inorganic Materials and Catalysis, Department of Chemical Engineering and Chemistry, Eindhoven University of Technology, 5612 AE Eindhoven, The Netherlands;* orcid.org/0000-0002-9754-2417; Email: e.j.m.hensen@tue.nl

Anja Bieberle-Hütter − *Electrochemical Materials and Interfaces (EMI), Dutch Institute for Fundamental Energy Research (DIFFER), 5612 AJ Eindhoven, The Netherlands;* orcid.org/0000-0001-8794-9312; Email: a.bieberle@differ.nl

Authors

Nitin P. Prasad − *Laboratory of Inorganic Materials and Catalysis, Department of Chemical Engineering and Chemistry, Eindhoven University of Technology, 5612 AE Eindhoven, The Netherlands; Electrochemical Materials and Interfaces (EMI), Dutch Institute for Fundamental Energy Research (DIFFER), 5612 AJ Eindhoven, The Netherlands;* orcid.org/0000-0003-1152-1664

Marcus Rohnke − *Institute for Physical Chemistry & Center for Materials Research, Justus Liebig University Gießen, 35392 Gießen, Germany;* orcid.org/0000-0002-8867-950X

Marcel A. Verheijen − *Plasma and Materials Processing (PMP), Department of Applied Physics, Eindhoven University of Technology, 5600 MB Eindhoven, The Netherlands;* orcid.org/0000-0002-8749-7755

Jacobus M. Sturm − *Industrial Focus Group XUV Optics, MESA+ Institute for Nanotechnology, University of Twente, 7522NB Enschede, The Netherlands;* orcid.org/0000-0002-0731-6329

Complete contact information is available at:
https://pubs.acs.org/10.1021/acsaem.3c01926

Notes

The authors declare no competing financial interest.

■ REFERENCES

(1) Intergovernmental Panel on Climate Change Climate Change 2022: Impacts, Adaptation and Vulnerability. 2022, https://www.ipcc.ch/report/ar6/wg2/ (accessed April 01, 2022).

(2) Howarth, R. W.; Jacobson, M. Z. How Green Is Blue Hydrogen? *Energy Sci. Eng.* **2021**, *9* (10), 1676−1687.

(3) Shaner, M. R.; Atwater, H. A.; Lewis, N. S.; McFarland, E. W. A Comparative Technoeconomic Analysis of Renewable Hydrogen Production Using Solar Energy. *Energy Environ. Sci.* **2016**, *9* (7), 2354−2371.

(4) van de Krol, R.; Grätzel, M. *Photoelectro-Chemical Hydrogen Production*; Springer, 2012.

(5) Sivula, K.; Van De Krol, R. Semiconducting Materials for Photoelectrochemical Energy Conversion. *Nat. Rev. Mater.* **2016**, *1* (2), 1−16.

(6) Kudo, A.; Miseki, Y. Heterogeneous Photocatalyst Materials for Water Splitting. *Chem. Soc. Rev.* **2009**, *38* (1), 253−278.

(7) Montoya, J. H.; Seitz, L. C.; Chakthranont, P.; Vojvodic, A.; Jaramillo, T. F.; Nørskov, J. K. Materials for Solar Fuels and Chemicals. *Nat. Mater.* **2017**, *16* (1), 70−81.

(8) Jiang, C.; Moniz, S. J. A.; Wang, A.; Zhang, T.; Tang, J. Photoelectrochemical Devices for Solar Water Splitting − Materials and Challenges. *Chem. Soc. Rev.* **2017**, *46* (15), 4645−4660.

(9) Xiao, M.; Luo, B.; Wang, Z.; Wang, S.; Wang, L. Recent Advances of Metal-Oxide Photoanodes: Engineering of Charge Separation and Transportation toward Efficient Solar Water Splitting. *Solar RRL* **2020**, *4*, No. 1900509.

(10) Yang, Y.; Forster, M.; Ling, Y.; Wang, G.; Zhai, T.; Tong, Y.; Cowan, A. J.; Li, Y. Acid Treatment Enables Suppression of Electron-Hole Recombination in Hematite for Photoelectrochemical Water Splitting. *Angew. Chem.- Int. Ed.* **2016**, *55* (10), 3403−3407.

(11) Cowan, A. J.; Tang, J.; Leng, W.; Durrant, J. R.; Klug, D. R. Water Splitting by Nanocrystalline TiO 2 in a Complete Photoelectrochemical Cell Exhibits Efficiencies Limited by Charge Recombination. *J. Phys. Chem. C* **2010**, *114* (9), 4208−4214.

(12) Zachäus, C.; Abdi, F. F.; Peter, L. M.; Van De Krol, R. Photocurrent of BiVO4 Is Limited by Surface Recombination, Not Surface Catalysis. *Chem. Sci.* **2017**, *8* (5), 3712−3719.

(13) Giménez, S.; Bisquert, J. *Photoelectrochemical Solar Fuel Production: From Basic Principles to Advanced Devices*; Springer: Cham, Switzerland, 2016.

(14) Bard, A. J.; Fan, F. R. F.; Gioda, A. S.; Nagasubramanian, G.; White, H. S. On the Role of Surface States in Semiconductor Electrode Photoelectrochemical Cells. *Faraday Discuss. Chem. Soc.* **1980**, *70* (0), 19−31.

(15) Baek, S. H.; Folkman, C. M.; Park, J. W.; Lee, S.; Bark, C. W.; Tybell, T.; Eom, C. B. The Nature of Polarization Fatigue in BiFeO3. *Adv. Mater.* **2011**, *23* (14), 1621−1625.

(16) Li, Z.; Wang, Y.; Tian, G.; Li, P.; Zhao, L.; Zhang, F.; Yao, J.; Fan, H.; Song, X.; Chen, D.; Fan, Z.; Qin, M.; Zeng, M.; Zhang, Z.; Lu, X.; Hu, S.; Lei, C.; Zhu, Q.; Li, J.; Gao, X.; Liu, J. M. High-Density Array of Ferroelectric Nanodots with Robust and Reversibly Switchable Topological Domain States. *Sci. Adv.* **2017**, *3*, No. e1700919, DOI: 10.1126/sciadv.1700919.

(17) Wang, H.; Liu, Z. R.; Yoong, H. Y.; Paudel, T. R.; Xiao, J. X.; Guo, R.; Lin, W. N.; Yang, P.; Wang, J.; Chow, G. M.; Venkatesan, T.; Tsymbal, E. Y.; Tian, H.; Chen, J. S. Direct Observation of Room-Temperature out-of-Plane Ferroelectricity and Tunneling Electroresistance at the Two-Dimensional Limit. *Nat. Commun.* **2018**, *9* (1), No. 3319.

(18) Lu, Z.; Yang, X.; Jin, C.; Li, P.; Wan, J.-G.; Liu, J.-M.; Lu, Z.; Yang, X.; Jin, C.; Wan, J.-G.; Liu, J.-M.; Li, P. Nonvolatile Electric-

Optical Memory Controlled by Conductive Filaments in Ti-Doped BiFeO3. *Adv. Electron Mater.* **2018**, *4* (2), No. 1700551.

(19) Allibe, J.; Fusil, S.; Bouzehouane, K.; Daumont, C.; Sando, D.; Jacquet, E.; Deranlot, C.; Bibes, M.; Barthélémy, A. Room Temperature Electrical Manipulation of Giant Magnetoresistance in Spin Valves Exchange-Biased with BiFeO 3. *Nano Lett.* **2012**, *12* (3), 1141−1145.

(20) Baek, S. H.; Jang, H. W.; Folkman, C. M.; Li, Y. L.; Winchester, B.; Zhang, J. X.; He, Q.; Chu, Y. H.; Nelson, C. T.; Rzchowski, M. S.; Pan, X. Q.; Ramesh, R.; Chen, L. Q.; Eom, C. B. Ferroelastic Switching for Nanoscale Non-Volatile Magnetoelectric Devices. *Nat. Mater.* **2010**, *9* (4), 309−314.

(21) Zhao, T.; Scholl, A.; Zavaliche, F.; Lee, K.; Barry, M.; Doran, A.; Cruz, M. P.; Chu, Y. H.; Ederer, C.; Spaldin, N. A.; Das, R. R.; Kim, D. M.; Baek, S. H.; Eom, C. B.; Ramesh, R. Electrical Control of Antiferromagnetic Domains in Multiferroic BiFeO3 Films at Room Temperature. *Nat. Mater.* **2006**, *5* (10), 823−829.

(22) Qiao, L.; Zhang, S.; Xiao, H. Y.; Singh, D. J.; Zhang, K. H. L.; Liu, Z. J.; Zu, X. T.; Li, S. Orbital Controlled Band Gap Engineering of Tetragonal BiFeO3 for Optoelectronic Applications. *J. Mater. Chem. C* **2018**, *6* (5), 1239−1247.

(23) Sando, D.; Carrétéro, C.; Grisolia, M. N.; Barthélémy, A.; Nagarajan, V.; Bibes, M. Revisiting the Optical Band Gap in Epitaxial BiFeO3 Thin Films. *Adv. Opt. Mater.* **2018**, *6* (2), No. 1700836.

(24) Song, J.; Kim, T. L.; Lee, J.; Cho, S. Y.; Cha, J.; Jeong, S. Y.; An, H.; Kim, W. S.; Jung, Y.-S.; Park, J.; Jung, G. Y.; Kim, D.-Y.; Jo, J. Y.; Bu, S. D.; Jang, H. W.; Lee, S. Domain-Engineered BiFeO3 Thin-Film Photoanodes for Highly Enhanced Ferroelectric Solar Water Splitting. *Nano Res.* **2018**, *11* (2), 642−655.

(25) Cao, D.; Wang, Z.; Nasori; Wen, L.; Mi, Y.; Lei, Y. Switchable Charge-Transfer in the Photoelectrochemical Energy-Conversion Process of Ferroelectric BiFeO3 Photoelectrodes. *Angew. Chem.- Int. Ed.* **2014**, *53* (41), 11027−11031.

(26) Ji, W.; Yao, K.; Lim, Y. F.; Liang, Y. C.; Suwardi, A. Epitaxial Ferroelectric BiFeO3 Thin Films for Unassisted Photocatalytic Water Splitting. *Appl. Phys. Lett.* **2013**, *103* (6), No. 062901.

(27) Wefring, E. T.; Einarsrud, M. A.; Grande, T. Electrical Conductivity and Thermopower of $(1 − x)$ BiFeO3 − XBi0.5K0.5-TiO3 $(x = 0.1, 0.2)$ Ceramics near the Ferroelectric to Paraelectric Phase Transition. *Phys. Chem. Chem. Phys.* **2015**, *17* (14), 9420−9428.

(28) Makarovic, M.; Kanas, N.; Zorko, A.; Ziberna, K.; Ursic, H.; Smabraten, D. R.; Selbach, S. M.; Rojac, T. Tailoring the Electrical Conductivity and Hardening in BiFeO3 Ceramics. *J. Eur. Ceram. Soc.* **2020**, *40* (15), 5483−5493.

(29) Lee, D. K.; Lee, D.; Lumley, M. A.; Choi, K. S. Progress on Ternary Oxide-Based Photoanodes for Use in Photoelectrochemical Cells for Solar Water Splitting. *Chem. Soc. Rev.* **2019**, *48*, 2126−2157, DOI: 10.1039/c8cs00761f.

(30) Das, S.; Fourmont, P.; Benetti, D.; Cloutier, S. G.; Nechache, R.; Wang, Z. M.; Rosei, F. High Performance BiFeO 3 Ferroelectric Nanostructured Photocathodes. *J. Chem. Phys.* **2020**, *153* (8), No. 084705.

(31) Shah, J. H.; Ye, H.-Y.; Liu, Y.; Idris, A. M.; Malik, A. S.; Zhang, Y.; Han, H.; Li, C. Exploration of the Intrinsic Factors Limiting Photocurrent Current Density in Ferroelectric BiFeO3 Thin Film. *J. Mater. Chem. A* **2020**, *8* (14), 6863−6873.

(32) Zhang, Z.; Tan, B.; Ma, W.; Liu, B.; Sun, M.; Cooper, J. K.; Han, W. BiFeO3 Photocathodes for Efficient H2O2 Production via Charge Carrier Dynamics Engineering. *Mater. Horiz.* **2022**, *9* (7), 1999−2006.

(33) Tan, B.; Reyes, A. M.; Menéndez-Proupin, E.; Reyes-Lillo, S. E.; Li, Y.; Zhang, Z. Full-Space Potential Gradient Driven Charge Migration inside BiFeO3Photocathode. *ACS Energy Lett.* **2022**, *7* (10), 3492−3499.

(34) Moniz, S. J. A.; Blackman, C. S.; Southern, P.; Weaver, P. M.; Tang, J.; Carmalt, C. J. Visible-Light Driven Water Splitting over BiFeO3 Photoanodes Grown via the LPCVD Reaction of [Bi(OtBu)-

3] and [Fe(OtBu)3]2 and Enhanced with a Surface Nickel Oxygen Evolution Catalyst. *Nanoscale* **2015**, *7* (39), 16343−16353.

(35) Papadas, I.; Christodoulides, J. A.; Kioseoglou, G.; Armatas, G. S. A High Surface Area Ordered Mesoporous BiFeO 3 Semiconductor with Efficient Water Oxidation Activity. *J. Mater. Chem. A* **2015**, *3* (4), 1587−1593.

(36) Liu, G.; Karuturi, S. K.; Chen, H.; Wang, D.; Ager, J. W.; Simonov, A. N.; Tricoli, A. Enhancement of the Photoelectrochemical Water Splitting by Perovskite BiFeO3 via Interfacial Engineering. *Sol. Energy* **2020**, *202*, 198−203.

(37) Radmilovic, A.; Smart, T. J.; Ping, Y.; Choi, K. S. Combined Experimental and Theoretical Investigations of N-Type BiFeO3 for Use as a Photoanode in a Photoelectrochemical Cell. *Chem. Mater.* **2020**, *32* (7), 3262−3270.

(38) Li, J.; Sha, N.; Zhao, Z. Effect of Annealing Atmosphere on the Ferroelectric Properties of Inkjet Printed BiFeO3 Thin Films. *Appl. Surf. Sci.* **2018**, *454*, 233−238.

(39) Wang, Y.; Zhang, M.; Yue, Y.; Zhang, H.; Mahajan, A.; Dunn, S.; Yan, H. Chemical Solution Deposition of Single-Phase BiFeO3 Thin Films on Transparent Substrates. *Solar RRL* **2022**, *6* (7), No. 2200124.

(40) Selbach, S. M.; Einarsrud, M. A.; Tybell, T.; Grande, T. Synthesis of BiFeO3 by Wet Chemical Methods. *J. Am. Ceram. Soc.* **2007**, *90* (11), 3430−3434.

(41) Zhang, T.; Shen, Y.; Qiu, Y.; Liu, Y.; Xiong, R.; Shi, J.; Wei, J. Facial Synthesis and Photoreaction Mechanism of BiFeO3/Bi2Fe4O9 Heterojunction Nanofibers. *ACS Sustainable Chem. Eng.* **2017**, *5* (6), 4630−4636.

(42) Das, S. C.; Katiyal, S.; Shripathi, T. Impedance Spectroscopy of Bi-Rich BiFeO3: Twin Thermal-Activations. *J. Appl. Phys.* **2018**, *124* (17), No. 174101.

(43) Lahmar, A.; Zhao, K.; Habouti, S.; Dietze, M.; Solterbeck, C. H.; Es-Souni, M. Off-Stoichiometry Effects on BiFeO3 Thin Films. *Solid State Ionics* **2011**, *202* (1), 1−5.

(44) Tian, S.; Wang, C.; Zhou, Y.; Li, X.; Gao, P.; Wang, J.; Feng, Y.; Yao, X.; Ge, C.; He, M.; Bai, X.; Yang, G.; Jin, K. Manipulating the Ferroelectric Domain States and Structural Distortion in Epitaxial BiFeO 3 Ultrathin Films via Bi Nonstoichiometry. *ACS Appl. Mater. Interfaces* **2018**, *10* (50), 43792−43801.

(45) Dedon, L. R.; Saremi, S.; Chen, Z.; Damodaran, A. R.; Apgar, B. A.; Gao, R.; Martin, L. W. Nonstoichiometry, Structure, and Properties of BiFeO3 Films. *Chem. Mater.* **2016**, *28* (16), 5952−5961.

(46) Yang, T.; Wei, J.; Guo, Y.; Lv, Z.; Xu, Z.; Cheng, Z. Manipulation of Oxygen Vacancy for High Photovoltaic Output in Bismuth Ferrite Films. *ACS Appl. Mater. Interfaces* **2019**, *11* (26), 23372−23381.

(47) Chen, X.; Zhang, H.; Wang, T.; Wang, F.; Shi, W. Optical and Photoluminescence Properties of BiFeO3 Thin Films Grown on ITO-Coated Glass Substrates by Chemical Solution Deposition. *Phys. Status Solidi A* **2012**, *209* (8), 1456−1460.

(48) Machado, P.; Scigaj, M.; Gazquez, J.; Rueda, E.; Sánchez-Díaz, A.; Fina, I.; Gibert-Roca, M.; Puig, T.; Obradors, X.; Campoy-Quiles, M.; Coll, M. Band Gap Tuning of Solution-Processed Ferroelectric Perovskite BiFe 1- x Co x O 3 Thin Films. *Chem. Mater.* **2019**, *31* (3), 947−954.

(49) Di, L.; Yang, H.; Xian, T.; Chen, X. Enhanced Photocatalytic Activity of NaBH4 Reduced BiFeO3 Nanoparticles for Rhodamine B Decolorization. *Materials* **2017**, *10* (10), 1118.

(50) Qi, J.; Kong, D.; Liu, D.; Pan, L.; Chen, Y.; Zhang, X.; Zou, J. J. Bimetallic Phosphide Decorated Mo−BiVO4 for Significantly Improved Photoelectrochemical Activity and Stability. *RSC Adv.* **2019**, *9* (27), 15629−15634.

(51) Li, J.; Guo, L.; Lei, N.; Song, Q.; Liang, Z. Metallic Bi Nanocrystal-Modified Defective BiVO4 Photoanodes with Exposed (040) Facets for Photoelectrochemical Water Splitting. *ChemElectroChem* **2017**, *4* (11), 2852−2861.

(52) Yang, B.; Jin, L.; Wei, R.; Tang, X.; Hu, L.; Tong, P.; Yang, J.; Song, W.; Dai, J.; Zhu, X.; Sun, Y.; Zhang, S.; Wang, X.; Cheng, Z.; Yang, B. B.; Jin, L. H.; Wei, R. H.; Tang, X. W.; Hu, L.; Tong, P.;

Yang, J.; Song, H.; Dai, M.; Zhu, X. B.; Sun, Y. P.; Zhang, S. J.; Wang, X. L.; Cheng, Z. X. Chemical Solution Route for High-Quality Multiferroic BiFeO3 Thin Films. *Small* **2021**, *17* (9), No. 1903663.

(53) Yamashita, T.; Hayes, P. Analysis of XPS Spectra of Fe2+ and Fe3+ Ions in Oxide Materials. *Appl. Surf. Sci.* **2008**, *254* (8), 2441–2449.

(54) Mills, P.; Sullivan, J. L. A Study of the Core Level Electrons in Iron and Its Three Oxides by Means of X-Ray Photoelectron Spectroscopy. *J. Phys. D: Appl. Phys.* **1983**, *16* (5), 723.

(55) Gomez-Iriarte, G. A.; Pentón-Madrigal, A.; de Oliveira, L. A. S.; Sinnecker, J. P. XPS Study in BiFeO3 Surface Modified by Argon Etching. *Materials* **2022**, *15* (12), 4285.

(56) Idriss, H. On the Wrong Assignment of the XPS O1s Signal at 531–532 EV Attributed to Oxygen Vacancies in Photo- and Electro-Catalysts for Water Splitting and Other Materials Applications. *Surf. Sci.* **2021**, *712*, No. 121894.

(57) Dupin, J. C.; Gonbeau, D.; Vinatier, P.; Levasseur, A. Systematic XPS Studies of Metal Oxides, Hydroxides and Peroxides. *Phys. Chem. Chem. Phys.* **2000**, *2* (6), 1319–1324.

(58) Yoon, D. H.; Tak, Y. J.; Park, S. P.; Jung, J.; Lee, H.; Kim, H. J. Simultaneous Engineering of the Interface and Bulk Layer of Al/Sol-NiOx/Si Structured Resistive Random Access Memory Devices. *J. Mater. Chem. C* **2014**, *2* (30), 6148–6154.

(59) Guan, S.; Hao, L.; Murayama, M.; Xie, X.; Komuro, S.; Zhao, X. Influence of Anneal Temperature in Air on Surface Morphology and Photoluminescence of ZnO Thin Films. *IOP Conf. Ser. Mater. Sci. Eng.* **2019**, *522* (1), No. 012004.

(60) Teraoka, Y.; Yoshimatsu, M.; Yamazoe, N.; Seiyama, T. Oxygen-Sorptive Properties and Defect Structure of Perovskite-Type Oxides. *Chem. Lett.* **1984**, *13* (6), 893–896.

(61) Kim, T.; Baek, G.; Yang, S.; Yang, J. Y.; Yoon, K. S.; Kim, S. G.; Lee, J. Y.; Im, H. S.; Hong, J. P. Exploring Oxygen-Affinity-Controlled TaN Electrodes for Thermally Advanced TaOx Bipolar Resistive Switching. *Sci. Rep.* **2018**, *8* (1), No. 8532.

(62) Lee, D.; Wang, W.; Zhou, C.; Tong, X.; Liu, M.; Galli, G.; Choi, K. S. The Impact of Surface Composition on the Interfacial Energetics and Photoelectrochemical Properties of BiVO4. *Nat. Energy* **2021**, *6* (3), 287–294.

(63) Bredar, A. R. C.; Chown, A. L.; Burton, A. R.; Farnum, B. H. Electrochemical Impedance Spectroscopy of Metal Oxide Electrodes for Energy Applications. *ACS Appl. Energy Mater.* **2020**, *3* (1), 66–98.

(64) Sinha, R.; Lavrijsen, R.; Verheijen, M. A.; Zoethout, E.; Genuit, H.; Van De Sanden, M. C. M.; Bieberle-Hütter, A. Electrochemistry of Sputtered Hematite Photoanodes: A Comparison of Metallic DC versus Reactive RF Sputtering. *ACS Omega* **2019**, *4* (5), 9262–9270.

(65) Klahr, B.; Gimenez, S.; Fabregat-Santiago, F.; Hamann, T.; Bisquert, J. Water Oxidation at Hematite Photoelectrodes: The Role of Surface States. *J. Am. Chem. Soc.* **2012**, *134* (9), 4294–4302.

(66) Man, S.; Leng, X.; Bai, J.; Li, Z.; Xu, L. Facile Synthesis of BiFeO3/Bi2O3 Composite Photocathode with Improved Photo-electrochemical Performance. *Mater. Lett.* **2022**, *323*, No. 132591.

(67) Yan, X.; Pu, R.; Xie, R.; Zhang, B.; Shi, Y.; Liu, W.; Ma, G.; Yang, N. Design and Fabrication of Bi2O3/BiFeO3 Heterojunction Film with Improved Photoelectrochemical Performance. *Appl. Surf. Sci.* **2021**, *552*, No. 149442.

(68) Chen, Z.; Liu, Z.; Zhan, J.; She, Y.; Zhang, P.; Wei, W.; Peng, C.; Li, W.; Tang, J. Resolving the Mechanism of Oxygen Vacancy Mediated Nonradiative Charge Recombination in Monoclinic Bismuth Vanadate. *Chem. Phys. Lett.* **2021**, *766*, No. 138342.

(69) Lamers, M.; Fiechter, S.; Friedrich, D.; Abdi, F. F.; Van De Krol, R. Formation and Suppression of Defects during Heat Treatment of BiVO4 Photoanodes for Solar Water Splitting. *J. Mater. Chem. A* **2018**, *6* (38), 18694–18700.

(70) Geneste, G.; Paillard, C.; Dkhil, B. Polarons, Vacancies, Vacancy Associations, and Defect States in Multiferroic ${\rm BiFeO}_3$. *Phys. Rev. B* **2019**, *99*, 24104.

(71) Xia, L.; Tybell, T.; Selbach, S. M. Bi Vacancy Formation in BiFeO 3 Epitaxial Thin Films under Compressive (001)-Strain from First Principles. *J. Mater. Chem. C* **2019**, *4870*, 4870.

(72) Liu, C.; Mao, S.; Shi, M.; Hong, X.; Wang, D.; Wang, F.; Xia, M.; Chen, Q. Enhanced Photocatalytic Degradation Performance of BiVO4/BiOBr through Combining Fermi Level Alteration and Oxygen Defect Engineering. *Chem. Eng. J.* **2022**, *449*, No. 137757.

(73) Wang, Z.; Guo, H.; Ning, D.; Ma, X.; Zheng, L.; Smirnov, D.; Sun, K.; Chen, D.; Sun, L.; Liu, X. Tuning Fermi Level and Band Gap in Li4Ti5O12 by Doping and Vacancy for Ultrafast Li+ Insertion/Extraction. *J. Am. Ceram. Soc.* **2021**, *104* (11), 5934–5945.

(74) Zhang, Q.; Valanoor, N.; Standard, O. Epitaxial (001) BiFeO3 Thin-Films with Excellent Ferroelectric Properties by Chemical Solution Deposition-the Role of Gelation. *J. Mater. Chem. C* **2015**, *3* (3), 582–595.